



# Fossilization of Precambrian microfossils in the Volyn pegmatite, Ukraine

Gerhard Franz<sup>1</sup>, Peter Lyckberg<sup>2</sup>, Vladimir Khomenko<sup>3</sup>, Vsevolod Chournousenko<sup>4</sup>, Hans-Martin Schulz<sup>5</sup>, Nicolaj Mahlstedt<sup>5</sup>, Richard Wirth<sup>5</sup>, Johannes Glodny<sup>5</sup>, Ulrich Gernert<sup>6</sup>, and Jörg Nissen<sup>6</sup>

<sup>1</sup>Institut für Angewandte Geowissenschaften, Technische Universität Berlin, 10587 Berlin, Germany

<sup>2</sup>Luxembourg National Museum of Natural History, 25 Rue Münster, 2160 Luxembourg, Luxembourg

<sup>3</sup>M.P. Semenenko Institute of Geochemistry, Mineralogy and Ore Formation, The National Academy of Sciences of Ukraine, 34, Palladina av., Kyiv, 03142, Ukraine

<sup>4</sup>Volyn Quartz Samotsvety Company, Khoroshiv (Volodarsk-Volynski), Ukraine

<sup>5</sup>Section 3.5: Interface Geometry, GFZ German Research Centre for Geosciences, Telegrafenberg, 14473 Potsdam, Germany

<sup>6</sup>Zentraleinrichtung Elektronenmikroskopie, Technische Universität Berlin, 10623 Berlin, Germany

**Correspondence:** Gerhard Franz (gefra548@gmail.com)

Received: 10 December 2021 – Discussion started: 21 December 2021

Revised: 23 February 2022 – Accepted: 24 February 2022 – Published: 31 March 2022

**Abstract.** We report on Precambrian microfossils from igneous rocks of the Volyn pegmatite district, associated with the Paleoproterozoic Korosten pluton, northwestern Ukraine. The fossils were recovered from meter-sized miarolitic cavities and show a well-preserved 3D morphology, mostly filamentous but with a large variety of types and also in irregular, flaky shapes reminiscent of former biofilms, as well as rare spherical objects. Based on literature data, pyrolysis experiments, and reflected light microscopy results, the organic matter (OM) is characterized as (oxy-)kerite. Further investigations with microscopic techniques, including scanning and transmission electron microscopy, and electron microprobe analysis show that fossilization likely occurred during a hydrothermal, post-pegmatitic event by silicification dominantly in the outermost 1–2  $\mu\text{m}$  of the microfossils. The hydrothermal fluid, derived from the pegmatitic environment, was enriched in  $\text{SiF}_4$ , Al, Ca, Na, K, Cl, and S. The OM shows O enrichment in which N and S content is low, indicating simultaneous N and S loss during anaerobic oxidation. Mineralization with Al silicates starts at the rim of the microfossils, continuing in its outer parts into identifiable encrustations and intergrowths of clay minerals, feldspar, Ca sulfate, Ca phosphate, Fe sulfide, and fluorite.

Breccias, formed during collapse of some the miarolitic cavities, contain decaying OM, which released high concentrations of dissolved  $\text{NH}_4^+$ , responsible for the late-stage for-

mation of tobelite-rich muscovite and buddingtonite. The age of the fossils can be restricted to the time between the pegmatite formation, at  $\sim 1.760$  Ga, and the breccia formation at  $\sim 1.49$  Ga. As the geological environment for the growth of the microorganisms and fossilization, we assume a geyser system in which the essential biological components C, N, S, and P for growth of the organisms in the miarolitic cavities were derived from microorganisms at the surface. Fossilization was induced by magmatic  $\text{SiF}_4$ -rich fluids. The Volyn occurrence is a distinct and uncommon example of Precambrian fossils, and the results underline the importance of cavities in granitic rocks as a possible habitat for microorganisms preserved in the deep biosphere.

## 1 Introduction

Precambrian fossils are rare, and their morphology is generally not well preserved. They occur mostly in (meta-)sedimentary rocks, but in recent years it became evident that pores, fissures, and other open spaces in igneous rocks can be a habitat for microorganisms (Ivarsson et al., 2020). In miarolitic cavities in pegmatites from the Volyn pegmatite district, Ukraine, genetically associated with the Paleoproterozoic Korosten pluton of the western Ukrainian shield (Fig. 1), fossils occur in a conspicuous filamentous

form. They are known as “kerite” and were first described by Ginzburg et al. (1987) as a result of abiogenic sublimation and polymerization of volatile hydrocarbons from the pegmatite. In Ukrainian–Russian literature this type of organic matter (OM) was characterized as (oxy-)kerite, i.e., highly mature OM. Gorlenko et al. (2000) and Zhmur (2003) were the first to re-interpret these kerites as fossils of filamentous cyanobacteria, based on electron microscopic investigations of ultra-thin sections. They also pointed out that cyanobacteria are not the only microorganisms, but they described the occurrence as a microbial community of an “Early Proterozoic autonomous biocoenosis”. Stable  $\delta^{13}\text{C}$  isotope ratios  $\leq -40\%$  of such filaments are similar to  $\delta^{13}\text{C}$  isotope ratios in methanogenic bacteria (Franz et al., 2017). Typical for kerite is the high N content, which goes up to 9 wt % (Luk’yanova et al., 1992; Franz et al., 2017). The maximum age of the fossils is restricted by the  $1760 \pm 3$  Ma intrusion age of the pegmatites (Shumlyansky et al., 2021; Fig. 1). The minimum age is constrained by  $^{40}\text{Ar}$ – $^{39}\text{Ar}$  laser-ablation age data of minerals in a breccia, which formed after consolidation of the pegmatites. This breccia contains degraded OM with newly formed muscovite (formation age  $1491 \pm 9$  Ma; Franz et al., 2021) and buddingtonite ( $\text{NH}_4$ -feldspar; minimum age of  $563 \pm 14$  Ma). Ammonium ions are a product of the degradation of OM, and the white mica age and the buddingtonite age restrict the age of the organisms most likely near to 1.5 Ga, the age of pseudomorph formation (for detailed discussion see Franz et al., 2022).

The miarolitic cavities hosting the kerite fossils (Fig. 2) are a special feature of these pegmatites, which are therefore referred to as “chamber pegmatites” (see reviews in Ivanovich and Alekseevich, 2007; Lyckberg et al., 2009). These chambers are zones of free growth for crystals (“crystal pockets”) and were formed in the cooling stage of the pegmatite in the same way as common miarolitic cavities, i.e., from magmatic fluids, liberated during crystallization. What is unusual is their size: Lyckberg et al. (2019) describe the largest pocket of pegmatite no. 521 at a depth of 96 m with dimensions of 45 m in length, up to 25 m in width, and about 20 m in height. Common are cavity dimensions of 4 to 6 m in length, 3 to 4 m in width, and 1 to 3 m in height (Ivanov and Alekseevich, 2007), and the unusually large size is attributed to the long cooling history on the order of millions of years of the Korosten pluton with supply of fluids from anorthositic magmas (Shumlyansky et al., 2021).

A striking feature of kerite is the well-preserved morphology (Zhmur, 2003; Franz et al., 2017), which poses the question of how the delicate OM without skeletal parts in the organisms was fossilized. Zhmur (2003)<sup>1</sup> interpreted this process as “hydrocarbon-aqueous fossilization” due to prolonged low-temperature dehydration and oxidation. Here we

<sup>1</sup>In the title of Zhmur, 2003, there is an obvious typing error: It says “Origin of Cambrian fibrous kerites of the Volyn region”, but in the text it is clear that the authors refer to a Precambrian age.

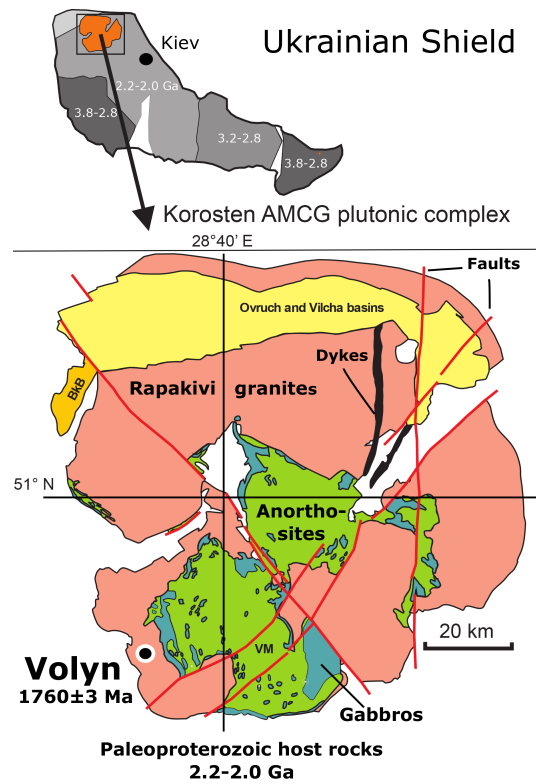


**Figure 1.** Location of the Volyn pegmatite field in the Korosten anorthosite–mangerite–charnockite–granite plutonic complex, northwestern Ukrainian Shield (numbers refer to the ages in Ga of consolidation of the shield; Shumlyansky et al., 2017). The pegmatite age of  $1760 \pm 3$  Ma at Volyn refers to zircon U–Pb SIMS (secondary ion mass spectrometry) data (Shumlyansky et al., 2021).

present data from reflected light microscopy, scanning electron microscopy (SEM), transmission electron microscopy (TEM), and electron probe microanalysis (EMPA) to show that the fossilization process is mainly driven by the reaction of Si–Al–(Ca) with the organisms via a fluid-phase rich in F, Cl, S, and P, followed by encrustation of Al silicates. Attempts to directly date black opal with inclusions of OM and of filamentous kerite using U–Pb systematics resulted, in the case of opal, in scattered U–Pb data indicative of open-system behavior. For the filamentous kerite we obtained a nominally Cambrian minimum age that is consistent with the inferred Precambrian age.

### Sample material and methods

Sample material from the Volyn pegmatite includes kerite, obtained from the Museum of the National Academy of Sciences, Semenenko Institute of Geochemistry, Mineralogy and Ore Formation, Kyiv, and seven kerite samples, sampled underground in situ from the pegmatites (Table 1). Kerite could not be found in the surrounding granite, only in the



**Figure 2.** (a) Kerite-rich in situ occurrence (black; arrows) on wall inside crystal cavity chamber in shaft 3 of Volyn Chamber Pegmatite, Volyn Piezo Quartz Deposit, Korosten Pluton, Zhitomirskaya Oblast, Ukraine, with chief geologist Vsevolod Chournousenko as scale. (b) Black kerite in situ on wall inside crystal cavity chamber. Photos courtesy of Vsevolod Chournousenko.

pegmatite. The microfossils are found free on the surface or partly in the upper layer of clay on the floor of the miarolitic open chamber (Fig. 2). Kerite occurs there in masses of kilograms and as described in the Russian and Ukrainian literature (Zmuhr, 2003, Gorlenko et al., 2000, and references therein), as verified by coauthor Vsevolod Chournousenko. It can be found also on the surface of beryl and topaz crystals.

In addition, we investigated single crystals of beryl with etch pits, which contain kerite, and used data from a previously investigated sample, 2008-V (Franz et al., 2017), a breccia collected from the mine tailings of pegmatite no. 2, which contains degraded OM in a pseudomorph after beryl, consisting of buddingtonite, muscovite, bertrandite, and opal. For the age determination, we used this OM with sample #9 (Table 1; aliquots a, b, c), which is topaz with degraded OM and black opal (sample BO, subdivided into aliquots), from the same shaft.

SEM images were obtained with a Hitachi SU8030 instrument, equipped with an EDAX element energy dispersive spectroscopy (EDS) system with a 30 mm<sup>2</sup> silicon drift detector (SDD) fitted with a silicon nitride window. We first tried to work without coating, but the filaments are non-conductive and were electrically charged. Samples were therefore coated with an approximately 5 nm thick Ir layer allowing for high-resolution imaging of the filaments' surfaces without a structure of the commonly applied Au coating. The kerite filaments without further cleaning or preparation were mounted on Al stubs stickered with conductive carbon tabs. The beryl crystals with kerite filaments were dust-cleaned with compressed air and coated with C.

The JEOL JXA-8530F field emission microprobe at TU Berlin was used to investigate the same mounts that were used for reflected light microscopy but with C coating for quantitative results and less absorbance (compared to Ir). Electron microprobe data for element distribution maps of cross sections or of parts of the rim of the filaments and flaky kerite in the wavelength dispersive mode of the microprobe were acquired using an 8 kV, 20 nA beam with a probe diameter of 64 nm. Backscattered electron (BSE) images were taken to select appropriate sites. Mappings were done in stage scan mode with pixel resolutions between 277 and 360 × 180 and 265, a pixel size of mostly 80 nm, and a dwell time per pixel of 200 ms. Total scan areas varied between 70 μm × 36 μm to 33.2 μm × 31.8 μm.

Open-system pyrolysis was performed using a Quantum MSSV-2 Thermal Analysis System© interfaced with an Agilent 6890 A gas chromatograph (GC). Milligram quantities (0.3–2.0 mg) of freshly powdered sample material were weighed into the central part of small glass capillaries and fixed with purified quartz wool that had been cleaned by heating at 630 °C in air for 30 min. Open-system pyrolysis was performed from 300 to 600 °C at 40 °C min<sup>-1</sup> in a flow of He at a rate of 30 mL min<sup>-1</sup>. The generated hydrocarbons were immediately transferred to a liquid-nitrogen-cooled trap and subsequently analyzed using an Agilent 6890 A gas chromatograph equipped with an HP-Ultra-1 column of 50 m length, 0.32 mm internal diameter, 0.52 μm film thickness, and flame ionization detector. The oven temperature was programmed from 30 to 320 °C at 5 °C min<sup>-1</sup>. Qualification of single compounds was conducted using reference chromatograms.

For the U–Th–Pb analysis, fragments of OM from two samples were selected under a binocular microscope. Fragments from sample #9 were visually pure, inclusion-free, and with a dark brownish color. Fragments from sample #1 showed fine-grained intergrowth with colorless to whitish phases, probably quartz and feldspar. After cleaning in double-distilled water in an ultrasonic bath, fragments (weight between 0.38 and 2.53 mg) were digested in 68 % HNO<sub>3</sub> at 220 °C for 48 h using a Parr-type hydrothermal digestion vessel, a procedure that has been shown to effectively mineralize a broad range of organic matter (Tahán et

**Table 1.** List of samples and their macroscopic appearance.

No./GFZ no.	Year of sampling	Material	Location	Kerite morphology comment
0/Museum Ac. Sci. Kyiv	Unknown	Kerite	Unknown	Filamentous
1/G017809	2018	Kerite	Shaft 3	Filamentous
2/G017810	2018	Kerite	Shaft 3	Filamentous
3/G017811	2018	Kerite	Shaft 3	Filamentous
4/G017812	2018	Kerite	Shaft 3	Filamentous, spherical
5/G017813	2013	Kerite	Shaft 3	Flaky, botryoidal
6/G017814	2013	Kerite	Shaft 3	Filamentous, flaky
7/G017815	2013	Kerite	Shaft 3	Filamentous, spherical
2008-V-10	2008	Beryl crystal with etch pits	Mine tailing pegmatite no. 2	Filamentous, spherical, flaky
9a, b, c	2018	Topaz with kerite	Shaft 3	Degraded kerite
BO	2018	Black opal	Shaft 3	Inclusions of OM
2008-V-1,a, b, c	2008	Pseudomorph after beryl	Mine tailing pegmatite no. 2	Degraded kerite

al., 1993). Optical control revealed that all OM was fully dissolved in this step. Sample solutions were dried and re-dissolved in 2% HNO<sub>3</sub>. Concentrations of U and Th were measured by isotope dilution with a Thermo Scientific Element XR ICP-MS at GFZ Potsdam, using a mixed <sup>235</sup>U–<sup>230</sup>Th spike. Concentrations of lead isotopes <sup>204</sup>Pb, <sup>206</sup>Pb, <sup>207</sup>Pb, and <sup>208</sup>Pb were determined with the same instrument from sample signal count rates compared to an external calibration curve for Pb. Corrections for background and for interference of <sup>204</sup>Hg on the <sup>204</sup>Pb signal were applied.

For TEM investigations foils were prepared using focused ion beam (FIB); for details of milling see Wirth (2004, 2009). The foils were studied in a Tecnai F20 X-Twin TEM operated at 200 kV with a field emission gun as electron source, equipped with a Gatan imaging filter (GIF Tridiem™), a Fischione high-angle annular dark field detector (HAADF), and an EDAX X-ray analyzer with an ultra-thin window. Bright field, dark field, and high-resolution TEM images are usually acquired as energy-filtered images applying a 20 eV window to the zero loss peak of the electron energy loss spectrum. Counting time for EDS analyses (processed with TIA™ software) in the scanning transmission mode across a pre-selected area, thus avoiding mass loss during the data acquisition, was 60 to 120 s. Electron diffraction data were acquired as selected area electron diffraction pattern (SAED) or derived from high-resolution lattice fringe images applying a fast Fourier transform (FFT). Electron energy loss spectra (EELS; data processing with Digital Micrograph™) were acquired in diffraction mode using a camera length of 700 mm. Applying a 1 mm entrance aperture the resulting acceptance semi-angle is 5 mrad. Dispersion was 0.1 eV per pixel, and acquisition time was 1 s.

## 2 Results

### 2.1 SEM images

The kerite morphology is best illustrated in SEM images (Fig. 3). There are three different types of morphologies, classified as filamentous and often branched (Fig. 3a and c), as spherical (Fig. 3b), and as irregular, flaky objects (Fig. 3c). Objects with spherical morphology are rare; therefore we restrict the study to the filaments and flakes which could also be found in thick sections of kerite embedded in epoxy and thus available for more detailed analytical investigations. Filaments are the dominant forms. Broken pieces are up to ~ 1 cm long and have a variable diameter, from 1–2 μm up to ca. 80 μm, mostly near ca. 15–20 μm. Many of the filaments are branched (Fig. 3d) or segmented (Fig. 3e and f) and show globular outgrowths, some of these outgrowths with botryoidal shape (Fig. 3e). This botryoidal shape can extend into more irregular, ridged forms. Flaky kerite is best seen in etch pits of beryl from Volyn (Fig. 3a and c), attached together with filamentous and rare spherical objects to the surface of beryl.

In many cases we see minerals grown onto the filaments, identified by chemical composition and shape as, for example, kaolinite and chlorite (Fig. 4a), as well as illite and Na–Al silicate (Fig. 4b); for documentation of the EDS spectra see Fig. S1 in the Supplement. On filaments with a rather smooth surface we see structures on the order of 100 nm × 500 nm which are enriched in Al, Si, Fe, and S, probably pyrite and/or marcasite with Si–Al incrustations (Fig. 4c). Segmented filaments (Fig. 4d) show larger structures, and the EDS analysis indicates incrustations of clay minerals such as illite and kaolinite. In many spectra, the peak of Ir is relatively broad, and this might be an indication for overlapping with a P peak. As we show later (results of EMPA), P is indeed present in the kerite rims. The matrix between filaments consists of opal, intergrown with silicates,

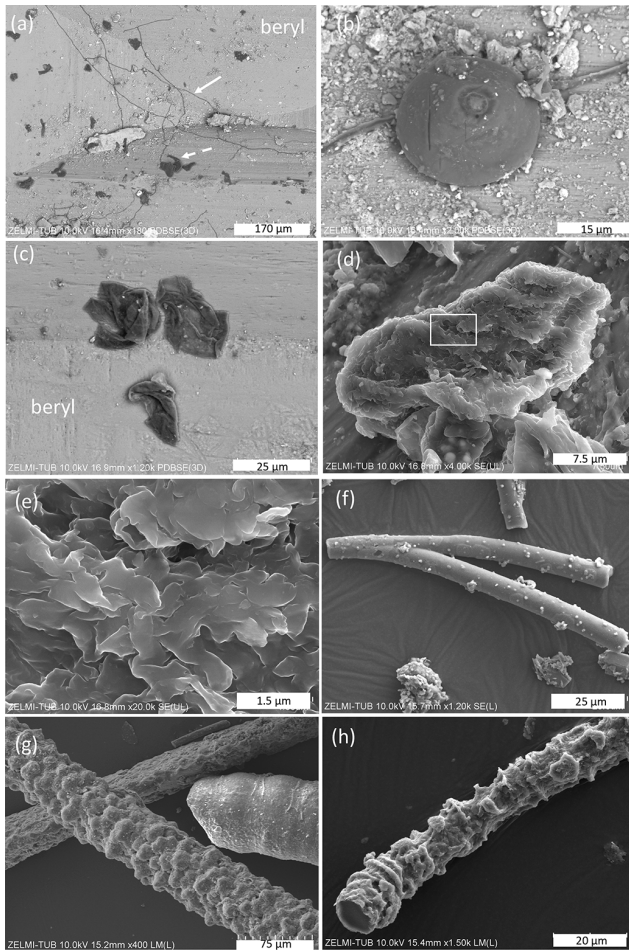


**Figure 3.** SEM images of kerite fossils, illustrating the different morphologies. (a) Filamentous and flaky kerite in etch pits of beryl (sample #10). (b) Spherical object on a filament (sample #10). (c) Flaky kerite (sample #10). (d, e) Enlarged particle of flaky kerite; white rectangle indicates position of (e). (f) Branched filament with smooth surface (sample #4). (g) Filaments with a botryoidal and a smooth, slightly segmented surface (sample #5). (h) Filament with a strongly segmented surface (sample #2). EDS spectra of flaky kerite are shown in Fig. S2 in the Supplement.

probably Na-feldspar, and clay minerals (Fig. 4e and f). In several cases, fluorite crystals could be identified, together with the incrustations. In this case, there are also traces of Ca in the incrustation.

The surface of botryoidal shapes (Fig. 5a) shows micrometer-wide gaps, explained as shrinking cracks, and ball-shaped outgrowths (Fig. 5b and c) with a dented surface, interpreted as a result of degassing of the OM. The EDS spectra of this surface shows peaks for Al and Si, in addition to the C–N–O content of kerite. The internal structure of kerite is seen in a broken face of a filament; it is characterized by a porosity (Fig. 5e, f, g, and h), also interpreted as the result of degassing. Individual pores are irregular in shape and on the order of several 100 nm large (Fig. 5g and h).

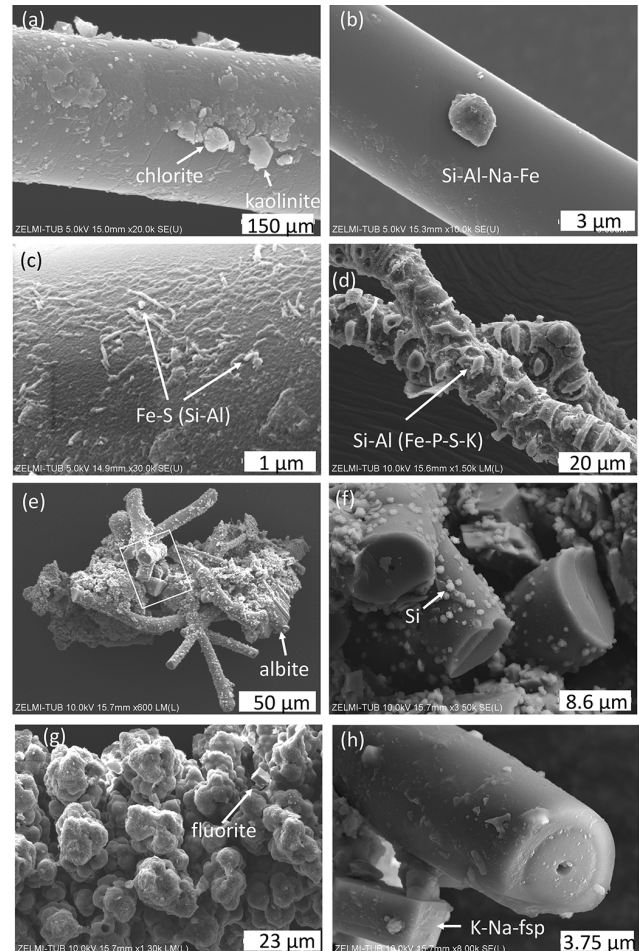


**Figure 4.** SEM images of minerals associated with kerite. (a) Chlorite and kaolinite and (b) unidentified Na–Fe–Al silicate grain grown onto a filament (sample #0). (c) High magnification of filament surface with Fe sulfide (pyrite/marcasite?) and incrustations of Si–Al (sample #0). (d) Incrustation on segmented filament, with dominantly Si–Al, minor peaks of Fe–P–S–K (sample #4). (e) Aggregate of filaments, cemented by minerals; lower right is an albite crystal; rectangle shows position of (f), enlarged part with broken filaments and small opal grains (identified by a Si peak and globular shape) attached to the surface (sample #4). (g) Aggregates forming a botryoidal surface of a filament, intergrown with a fluorite crystal. (h) Alkali feldspar, grown onto a broken filament with central cavity.

In cross section, some of the broken filaments show a central cavity, i.e., a channel extending along the filament axis (Figs. 4h and 6). The cross sections of this channel vary from ca. 250 nm × 500 nm (Fig. 6a) to ca. 20 μm × 20 μm (Fig. 6f) in diameter. In some cases, the channel has a six-sided outline (Fig. 6f, g, and h). The fractured surface with fringe fractures, sub-perpendicular to the filament length (Fig. 6a and g), indicates brittle behavior of the filaments, which was also observed during handling of the individual filaments for preparation. Figure 6d shows a broken filament with a sheath-like

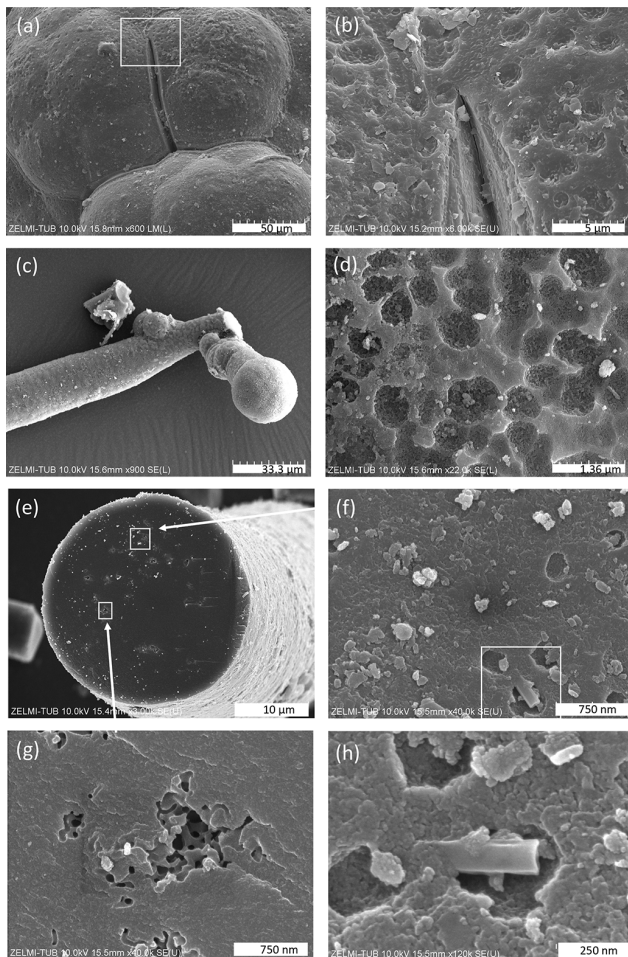


**Figure 5.** SEM images of surfaces of kerite. (a) Botryoidal surface with a shrinking crack; inset shows enlarged part in (b) with a dented surface (sample #5). (c) Ball-shaped end of a filament with (d) dented surface (sample #1). (e) Broken filament (sample #3) showing internal porosity (f, g, h) with irregular outlines a few hundreds of nanometers wide. White rectangle in (f) indicates enlarged part shown in (h).

outer part. The outer rim (with a dented surface, seen in its lower part) contains some Al–Si, a small amount of K, and possibly P (Fig. S4 analyses 2 and 5 in the Supplement); the inner rim shows only traces of Al–Si but some U (analyses 3 and 4), whereas the center near to the channel (analysis 6) shows only the peaks of C–N–O, characteristic for kerite. The count ratios for C/O increase systematically from outer rim to the center (Fig. S4).

## 2.2 Reflected light microscopy

In two-dimensional cuts in polished mounts in epoxy and observed under UV light for fluorescence and under white light for reflectivity (Fig. 7), the clear outer circular (to elliptical in oblique sections) shape of filaments is obvious in cross sections (Fig. 7a). In longitudinal sections (Fig. 7b), the

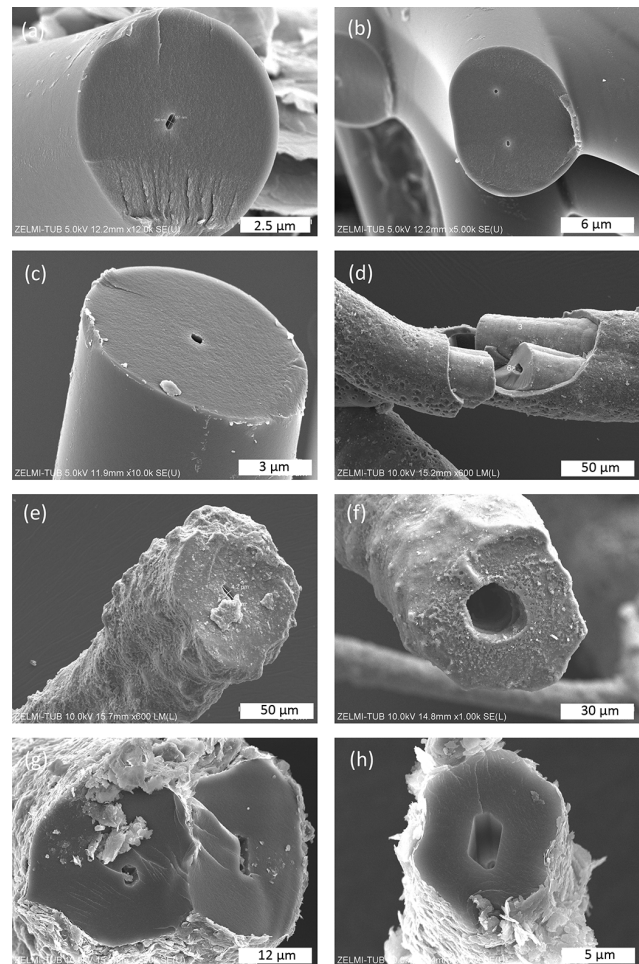


**Figure 6.** SEM images of broken filaments showing a central channel. (a) Six-sided channel with dimensions  $260\text{ nm} \times 550\text{ nm}$  of filament with a smooth surface and fringe fractures on the broken face, indicating brittle behavior. (b) Double channel, probably initial crosscutting of a branching (cf. Fig. 4d). (c) Similar channel as in (a) but with a less regular outline (all sample #0). (d) Filament with a central part, a sheath-like outer part, and a channel; numbers refer to analysis points (see text; EDS spectra in Fig. S4). Note dented surface in lower part of the sheath-like outer part (sample #5). (e) Filament with a rough surface and a channel  $4\text{ }\mu\text{m} \times 11\text{ }\mu\text{m}$ . (f) Large, ca.  $25\text{ }\mu\text{m}$  wide channel with six-sided outline (both sample #5). (g, h) Filaments with encrustations of clay minerals and six-sided channels (sample #7).

symmetrical internal structure, which shows up in the cross sections, extends along the whole filament. There are mainly three zones: an outer discontinuous, thin rim with a higher reflection and lower luminescence (zone 1), followed by a zone 2 with poorer reflection and higher fluorescence, and a core zone 3 with low fluorescence and intermediate reflectivity. The central, open channel with a different width is also seen in many filaments (Fig. 7a). Ball-shaped outgrowths show the same type of zoning as the filaments. Flaky kerite is seen as a thin (a few micrometers wide) (?bio-)film intergrown

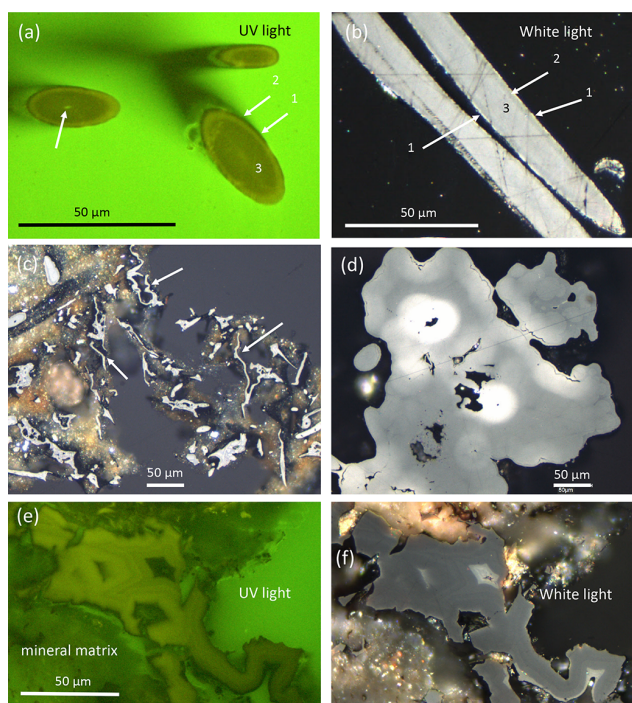


**Figure 7.** Optical reflected light microscopy of polished grain mounts under UV light for fluorescence and under white light for reflectance. **(a)** Cross section of filaments with a central channel (left arrow) and three zones of fluorescence. **(b)** Longitudinal sections show a symmetrical distribution of the three zones in reflectance, in which the rim with high reflectance corresponds to the rim with low fluorescence shown in **(a)**. **(c)** Thin flaky kerite, interpreted as former biofilms (arrows). **(d)** Botryoidal kerite with zonal distribution of reflectivity. **(e, f)** Thick masses of flaky kerite with zonal fluorescence and reflectivity.

with mineral matrix (Fig. 7c). Botryoidal shapes show difference in reflectivity which runs parallel to the surface (Fig. 7d) and with highest reflectivity around pores. Thick, irregularly shaped masses, possibly degraded OM (Fig. 7e and f), show rims high in reflectance and zonal distribution of luminescence in UV light.

### 2.3 Electron microprobe analyses (EMPA)

The same mounts prepared for reflected light microscopy were used for EMPA. Within the mineral matrix, we confirmed the presence of fluorite, closely intergrown with kerite, and also identified buddingtonite, characterized by zoning and a significant decrease in the  $\text{NH}_4$  component from core to rim (Fig. S4).

In order to show the distribution of elements in kerite by element mapping with EMPA, we chose two cross sections of filaments (Fig. 8): the outer part of a large, segmented filament (Fig. 9), and a botryoidal part with ball-shaped outgrowths on more irregularly shaped kerite (Fig. 10), as well as the rim of flaky kerite (Fig. 11). BSE images for location

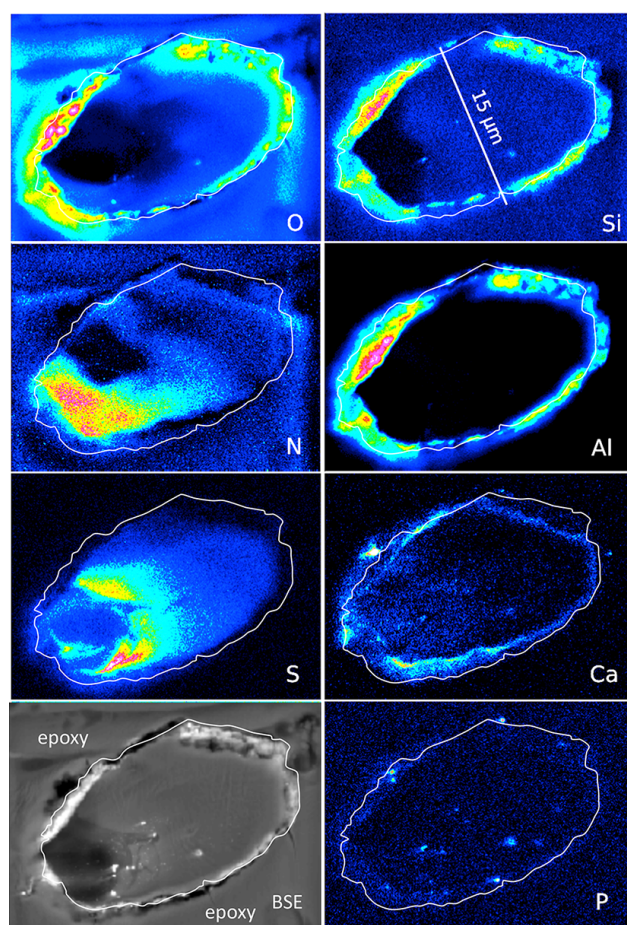


**Figure 8.** Element distribution (EMPA) of an oblique section of a 15  $\mu\text{m}$  wide filament embedded in epoxy. White line indicates outermost rim of the filament, as seen in the BSE image. BSE contrast is lowest in the area of low O and high N content. Si and Al (with O) form an outer rim, indicating Al silicates (probably clay minerals, as determined by SEM). Ca is also concentrated in the rim but also in spots, together with P, and in the area with high S. Scanning conditions: pixel resolution of  $360 \times 265$ , pixel size of 80 nm, dwell time per pixel of 200 ms, total scan area  $28.8 \mu\text{m} \times 21.2 \mu\text{m}$ .

of the mapping areas in the selected grains are shown in the Fig. S5 in the Supplement. Mapping included the characteristic elements identified before with SEM-EDS, i.e., O–N as part of kerite (C was not mapped because samples were C coated), S and P, which can be part of kerite but were also observed on the surface as sulfate or phosphate minerals (see above, SEM investigations), and Si, Al, and Ca as characteristic for silicates. Cl was mapped because we found it also on the surface of the OM in the etch pits in EDS analysis but was below detection level in the element distribution maps. Because the OM is very sensitive to the electron beam (see image after mapping in Fig. S5c), we chose a trade-off between high resolution, X-ray excitation, and measuring time, but nevertheless, beam-related damage could not be completely avoided.

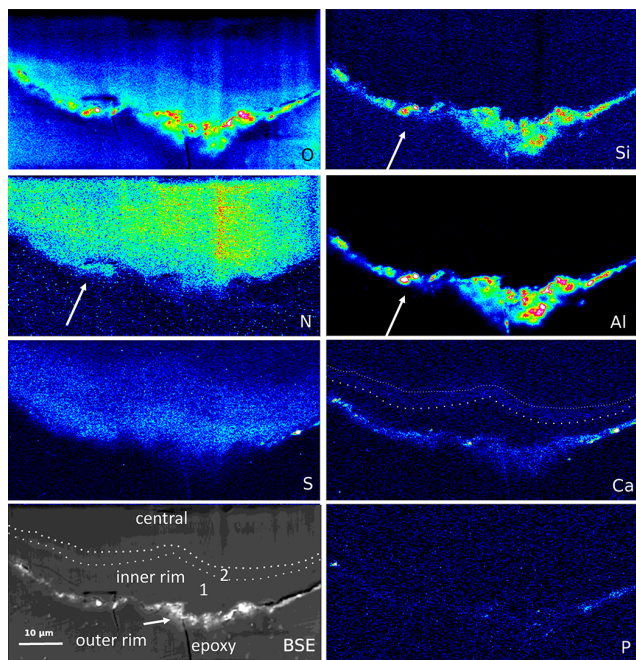


**Figure 9.** Element distribution (EMPA) of the rim of a large filament. The rim consists of three areas, best visible in the BSE and Ca image: an outer, irregular, and discontinuous rim with enrichment of Si–Al–O and Ca, an inner rim 1, poor in Ca, followed by an approximately 1–2 µm wide inner rim 2, enriched in Ca (dotted lines). In the outer rim, Ca is also concentrated, together with P and S. N distribution is relatively homogeneous but notably extends up to the outer rim, together with Al–Si (arrows), indicating formation of NH<sub>4</sub> minerals (buddingtonite, tobelite). Vertical stripes are due to beam damage. Scanning conditions: pixel resolution 350 × 180 with pixel size of 200 nm and a dwell time per pixel of 200 ms; total scan area 70 µm × 36 µm.

An oblique section of a 15 µm wide filament (Fig. 8) shows O enriched in the upper-right part, where N and S are low, indicating simultaneous N and S loss during progressive maturation. During maturation of OM labile nitrogen- and sulfur-bearing compounds are converted and lost, whereas oxygen-bearing macromolecules are enriched (Poetz et al., 2014). Here, mineralization of the organic fraction was preservative due to aromatization, and this process caused formation of oxygen-bearing aromatic macromolecules. However, S is low in the area in the lower left with the lowest BSE contrast and where N is concentrated. Si and Al concentrated in the outer, irregular, and discontinuous rim, together with O, present as Al silicates as determined by SEM. The Ca distribution is complex; it is enriched in the rim but does not follow Si–Al. Instead, it forms an inner rim. It is also concentrated in the lower-left part of this filament, in the same area where S is enriched. P shows some enrichments in spots in the inner part and in the rim, together with Ca interpreted as Ca phosphate. Similar element distributions were observed in a circular section of a filament (Fig. S6 in the Supplement).

The outer rim of a segmented filament (Fig. 9) allows a sharper differentiation compared to the observations above: Si, Al, and O are concentrated in the outer, irregular, and discontinuous rim, together with Ca, which is enriched in spots, together with P but also with S (probably forming Ca sulfate); S is enriched, together with Ca, in the outer rim. The outer rim is followed by an inner rim 1, poor in Ca, and then by an inner rim 2 with Ca enrichment. O distribution is highest in the outer rim, high in the inner rim 1 with a rather sharp boundary to the inner rim 2, and then diffuse into the central part. N shows a relatively homogeneous distribution but occurs up to the outer rim in areas of Si–Al concentrations, indicating the formation of NH<sub>4</sub> minerals (buddingtonite, tobelite).

The element distribution in botryoidal kerite (Fig. 10) is characterized by an internal, heterogeneous N distribution, anticorrelated with O, which is visible in the BSE contrast. Sulfur systematically decreases from the central part towards the rim. Calcium is enriched in a thin rim, associated with P in a few spots as Ca phosphates. The element distribution in flaky kerite (Fig. 11) is generally similar to the observations made in filaments. Al silicates form an outer, discontinuous rim, Ca is slightly above the background in the rim but also forms discrete, small ( $\leq 1$  µm) Ca sulfates and Ca phosphates. Sulfur is absent (except for the enrichment in Ca sulfates) in this rim, indicating loss of S during maturation and fossilization. Towards the interior of the flaky OM, distribution of N, O, and S is heterogeneous, a possible indication for a primary (biological) character, combined with loss of N during degradation. A different flaky object shows similar element distributions (Fig. S8 in the Supplement); however the phosphatization in the outermost rim is more pronounced than in the other element distribution maps.

## 2.4 TEM investigations

TEM investigations of FIB-cut foils from a filament, with the foil cut parallel to the elongation of the filament. In the center (Fig. 12) it shows the amorphous character and the presence of Si, together with C–N–O–S. In the rim, infiltration of Si, Al, and Ca, but in addition also Mg, Fe, K, and Ni in the whole filament, could be confirmed (Fig. S8); N was also confirmed by EELS analysis (Fig. S8) in the dominantly C-rich matrix.

## 2.5 Pyrolysis

Results of open-system pyrolysis are consistent with other observations, indicating mature or very mature OM, and there is no essential difference between samples with well-preserved shape and others with many incrustations. The gas chromatographic fingerprints of sample #0 are shown in Fig. 13, and the results of the other samples are in Fig. S9 in the Supplement.

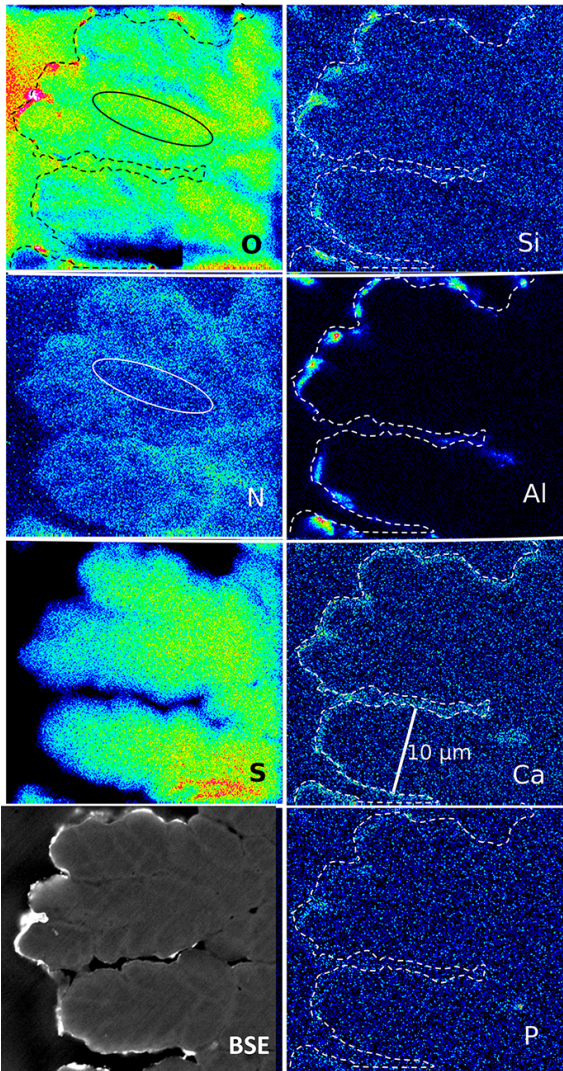


**Figure 10.** Element distribution (EMPA) in botryoidal kerite. The rim (dashed line) is outlined as seen in the BSE image. Si, Al, and O are concentrated in a discontinuous rim, indicating Al silicates. Ca is concentrated in spots in this rim, together with P, indicating Ca phosphate. Sulfur decreases systematically from the central part to the rim. N distribution is heterogeneous and mimics the BSE contrast. Areas rich in O are poor in N (see oval outlined area). Scanning conditions: pixel resolution of  $277 \times 265$  with pixel size of 120 nm and a dwell time per pixel of 200 ms; total scan area  $33.2 \mu\text{m} \times 31.8 \mu\text{m}$ .

All are strongly dominated by hydrocarbon gases  $C_{1-5}$  (methane through pentane) and subordinately by alkylated mono- and diaromatic compounds. These are typical pyrolysis breakdown products of organic matter in general, but as higher  $n$ -alkyl homologues ( $n-C_{6+}$ ) or oxygen-, sulfur-, and nitrogen-functionalized compounds (e.g., phenols, thiophenes, and carbazoles) as indicators of biological precursor structures (Larter, 1984; Horsfield, 1989; Sinninghe Damsté et al., 1989) are essentially absent, they are indicative of ma-

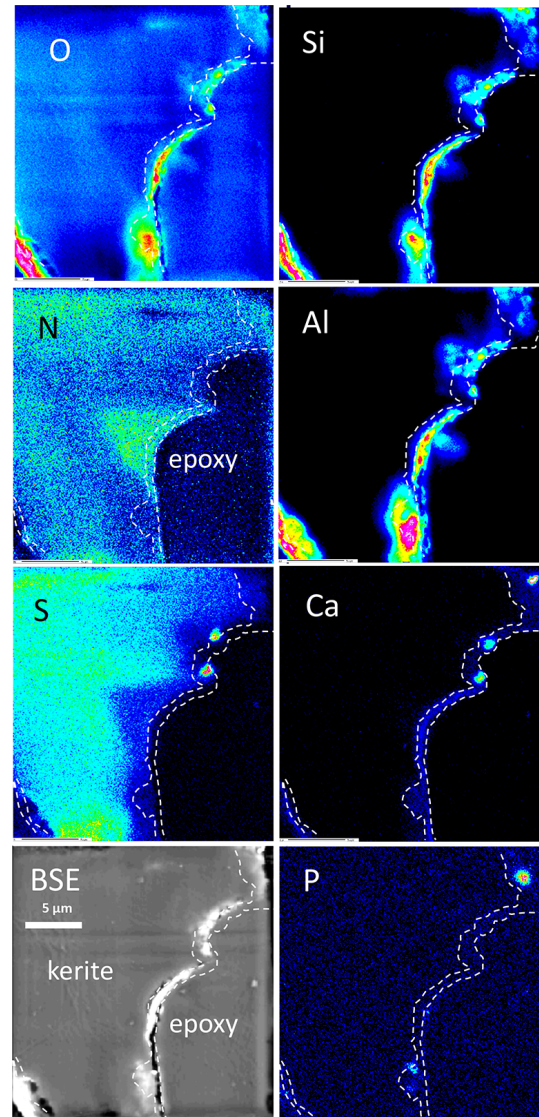


**Figure 11.** Element distribution (EMPA) of the rim of flaky kerite. The rim is outlined as seen in the Ca image. Si, Al, and O are concentrated in a discontinuous rim, indicating Al silicates. Ca is concentrated in spots, together with P and S, indicating Ca sulfates and Ca phosphates but also in a continuous rim with concentrations slightly above the background. Sulfur – except for the enrichment in spots – is absent in this area and also less concentrated near to the rim. N distribution is heterogeneous, but as in Fig. 9 it can extend up to the outer rim. Areas rich in N are poor in O.

ture OM. Loss of functional groups during diagenesis and loss of H-rich components during catagenesis leads all organic matter types to move towards the point (metagenesis) where they become indistinguishable, finally possessing only a potential for the generation of dry gas (methane) and monoaromatic compounds (Tissot and Welte, 1984; Quigley and Mackenzie, 1988; England and Mackenzie, 1989; Horsfield, 1989). In line with remaining fluorescence the composition

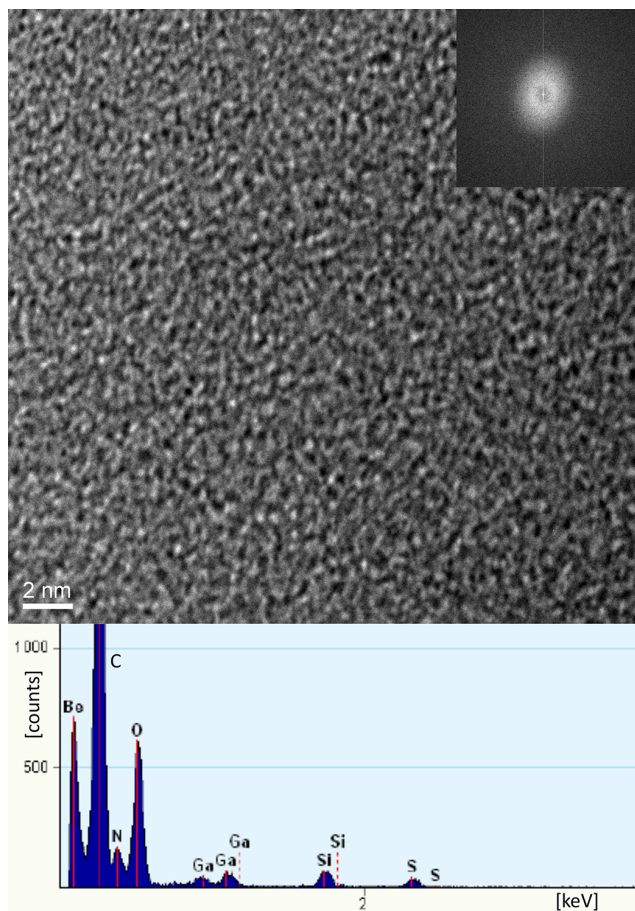


**Figure 12.** HRTEM image of central part of a filament showing amorphous kerite (inset is electron diffraction pattern) and EDS spectrum of a spot, confirming Si as an impurity and C–N–O and S as the kerite constituents. Ga peak is from the cutting of the FIB foil, and Be is from the Be sample holder.

of the pyrolysate, especially the presence of wet gases ( $C_{2-5}$ ) and diaromatic compounds, indicates that the OM has not yet arrived at metagenesis ( $R_o > 2.0\%$ , where  $R_o$  = vitrinite reflectance in oil; Tissot and Welte, 1984). GC fingerprints resemble, for example, those of Paleozoic coals and shales from Australia at  $1.7\% < R_o < 2.3\%$ ; Mahlstedt et al., 2014, 2015). Assuming typical geological heating rates between 1 and  $3 \text{ K Myr}^{-1}$  and based on the easy $R_o$  model (Burnham and Sweeney, 1989), OM at these maturity levels must have been heated to somewhere between 175 and  $200^\circ\text{C}$ ; a similar temperature range was also derived from mineral equilibria (Franz et al., 2017). In the case that peak temperatures were very short-lived, temperatures could have been slightly higher, but the time duration for the maturation of the Precambrian fossils is essentially unknown.

## 2.6 U–Th–Pb analyses

Results of Pb isotope analyses of kerite samples #9 and #1 and the OM from the pseudomorph sample are listed in Table 2 and shown in Fig. 14. The reference line corresponds to an age of 493.2 Ma, however with a large uncertainty of  $\pm 97.8 \text{ Ma}$  ( $1\sigma$ ). The apparent age is considered as a minimum age because OM is very susceptible for U, which has likely been present in the fluids circulating in the pegmatitic environment since the formation of the miarolitic chambers until modern times, a process that is capable of continuously resetting U–Pb dates.

Chemical and U, Th, and Pb isotope data of black opal are presented in Tables S1 to S3 in the Supplement. Major element analyses (Table S1) in opal indicate approximately 2.5 wt % undetermined elements, likely  $\text{H}_2\text{O}$  and hydrocarbons. Minor elements are Al (up to 1 wt %  $\text{Al}_2\text{O}_3$ ), Na, Ca, and Fe, which are present in 0.1 to 0.3 wt % oxide, whereas Ti, K, Mg, Fe, Cr, V, and Mn occur in smaller amounts. The heterogeneous distribution of elements is also seen in the trace element content among the three aliquots; Ba, Be, Li, Rb, Sc, Sr, Th, U, V, Zn, and Zr stand out with content each above  $1 \mu\text{g g}^{-1}$  in some of the aliquots. The U–Th–Pb isotope data (Table S3) indicate open-system behavior also for the black opal. The data show a large scatter; only two sample pairs allowed old  $^{208}\text{Pb}/^{232}\text{Th}$  ages of  $1500 \pm 46 \text{ Ma}$  and  $1279 \pm 35 \text{ Ma}$ , respectively, to be calculated.

## 3 Discussion

### 3.1 Fossilization process

A further determination of the exact nature of the excellently preserved microbial fossils requires a distinction between primary features, i.e., biological, and secondary features, i.e., those produced by fossilization. The nature of the fossils (bacteria, archaea, or fungi) which colonized the igneous rocks has not yet been clarified; it requires more research, also with more details on spherical kerite, which is in progress.

Kerite is highly mature, as shown by pyrolysis experiments (Fig. 13), but has not transformed into graphite, as shown by TEM investigations. It is completely amorphous (see in high-resolution transmission electron microscopy (HRTEM) image; Fig. 12), indicating rather low temperatures during fossilization and afterwards. This is also consistent with the observation that thin filaments are not completely opaque but dark-brown transparent, confirming Luk'yanova et al.'s (1992) observations. Their X-ray data of kerite showed a diffuse maximum at ca.  $8^\circ\theta$ , interpreted as a mixture of different carbohydrates with O, N, and S, some graphite-like sheets, hexamethylene, and polymerized carbohydrates with O. The fringe fractures (Fig. 6a) show that the filament behaved brittlely; i.e., the whole filament has

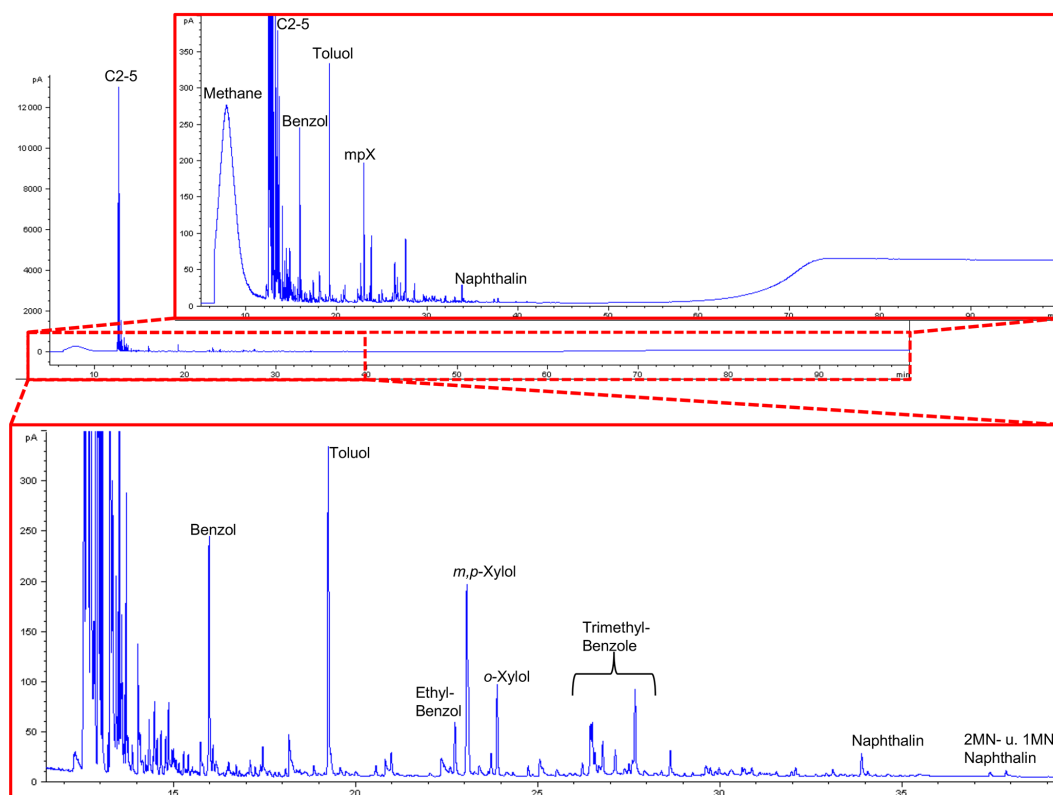


**Figure 13.** GC traces from open-system pyrolysis of kerite (sample #0/Museum Ac. Sci. Kiev) are dominated by the hydrocarbon gases methane through pentane and subordinately by alkylated mono- and diaromatic compounds, typical breakdown products of mature or very mature OM.

**Table 2.** Results of Pb isotope data of aliquots of OM: sample #9 (visually pure oxykerite) and sample #1 (impure with whitish minerals; RSD signifies relative standard deviation).

Sample	Weight (g)	$^{206}\text{Pb}/^{204}\text{Pb}$	RSD %	$^{206}\text{Pb}/^{207}\text{Pb}$	RSD %	$^{208}\text{Pb}/^{204}\text{Pb}$	RSD %
UKR 1 9-a	0.00253	477.3	5.3	42.83	10.63	5.32	108.5
UKR 2 9-b	0.00090	36.46	3.5	17.04	2.132	2.01	42.46
UKR 3 9-c	0.00101	320.2	10.2	33.39	8.925	4.78	85.19
UKR 4 1-a	0.00038	51.00	0.9	18.45	2.753	1.61	70.18
UKR 5 1-b	0.00043	53.22	1.5	18.61	2.870	1.07	73.17
UKR 6 1-c	0.00067	47.43	0.9	18.01	2.634	1.41	64.14

reached a similarly high degree of aromatization, which relates to high thermal maturity (Dormans et al., 1957; Oberlin et al., 1974; Radke et al., 1997).

Alteration by progressive maturation (e.g., the oxygen pattern along interfaces or affecting the whole kerite matrix) as a major feature is also seen in the element distribution (Figs. 8–11). Sulfur can form Ca sulfates, as seen in micrometer-sized spots in the rim, but is generally decreased towards the rim; more detailed mapping of the element distribution in the outer rim area shows Ca enrichment in spots parallel with S but also with P (Figs. 9 and S7 in the Supplement), and we speculate about the presence of both Ca sulfate and Ca phosphate nanoscale inclusions due to infiltration of Ca

and reaction with S and P. Sulfur and P were transported out of the filament, and reaction with Ca produced the Ca-free inner rim 1. Transport of Ca went further into the filament producing the inner rim 2. Phosphatization, a common fossilization process (e.g., Briggs, 2003), is thus only a minor feature. Alternatively, the Ca distribution in the outer part of the filament might mimic a primary feature, preserved from their growth.

The distribution of Si–Al (together with O) is most conspicuous and restricted to a rim of  $\sim 1\text{--}2\ \mu\text{m}$  width (Figs. 8–11). The presence of Si–Al is confirmed by analytical data with SEM (Fig. 6d) and TEM (Fig. 12) and suggests that silicification is the first-order process of fossilization. The

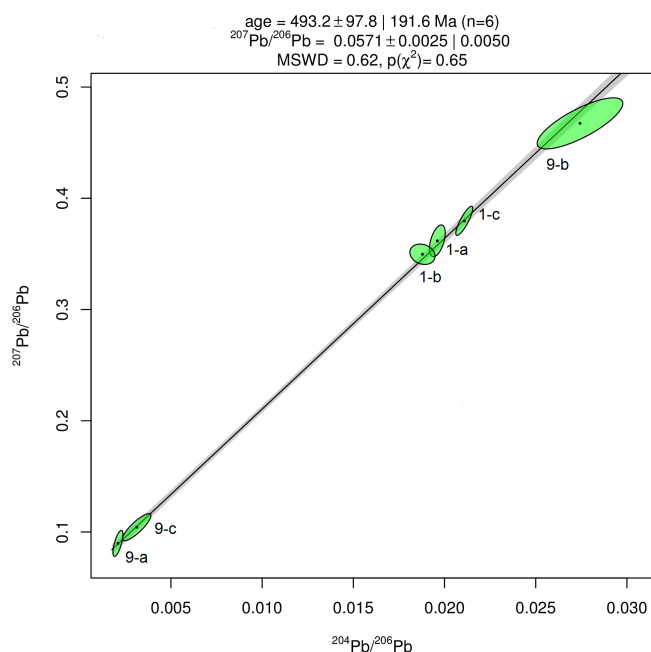


**Figure 14.** Results of Pb–Pb age determination of kerite from Volyn pegmatite. The reference line corresponds to an age of  $493.2 \pm 97.8$  Ma ( $1\sigma$ ). The large uncertainty is mainly due to very small amounts of Pb in the samples, resulting in poor ion counting statistics in mass spectrometry. Data were plotted and age calculated using the program IsoplotR (Vermeesch, 2018).

patchy distribution indicates the formation of Al silicate minerals, probably kaolinite or related phases. These patches were observed on the surface of the filaments as vermicular structures (Fig. 4c), some with clear development of crystal faces (Fig. 4a) continuing into more coarse-grained features, which we call encrustations (Fig. 4d). Finally, the patches change into intergrowths of minerals, which could be characterized by shape and chemistry as alkali feldspar, clay minerals, opal, Fe sulfides, and fluorite (Fig. 4e, f, g, and h).

We interpret the porosity observed on the surface of botryoidal structures and ball-shaped outgrowths on filaments (Fig. 5c and d) and on a broken cross section (Fig. 5e, f, g, and h) as degassing features. The irregular internal pores on the scale of a few hundred nanometers indicate irregular pathways of the gas, transitional towards the outer part into more regular, circular, and larger pores of 1 to 2  $\mu\text{m}$  in diameter. We interpret cracks in the surface (Fig. 5a and b) as a shrinking phenomenon and the irregular shape of flaky kerite on the etch pits of beryl (Fig. 3a and c) as a shrinking phenomenon of a formerly coherent biofilm. The outgrowths and ball-shaped ends of filaments were interpreted by Zhmur (2003) as spherical swellings of the filament sheaths produced by degassing. However, their size and transition to botryoidal and dented structures (Fig. 5) are more consistent with an interpretation as a primary feature because we do not see an easy way to produce these features by fossiliza-

tion. In addition, the cross sections (Fig. 7) of these structures with regular outline of, for example, the distribution of fluorescence and the mappings (Fig. 10) also indicate a primary feature. In contrast, the more irregular, ridge-like features (Fig. 3d) covered with platy clay minerals such as kaolinite (Figs. 3 and 6g and h) seem to represent strongly modified, original segmentation of the filaments during the fossilization process.

Many, but not all, of the broken filaments show a central channel (Fig. 6), visible also in BSE images of embedded filaments in cross sections, and it is the question of whether this is a primary or a secondary fossilization feature. In small nanometer-scale channels, the ratio of the solid outer part to the channel is  $\approx 10 : 1$  (in cross section, see Fig. 6a and c), and, together with the observation that not all filaments have this channel, it might be interpreted as a shrinking phenomenon. However, in micrometer-sized channels the ratio goes down to  $\approx 1 : 1$  (Fig. 6f and h), and such a high loss of material during degassing seems unlikely. Furthermore, the six-sided outline, seen in small and large channels, cannot be explained by shrinking. There is no reason why a cylindrical body during shrinking should open a central channel with a regular outline.

In order to describe the infiltration process for the fossilization and the responsible fluid phase, it is important to note that kerite occurs not only with the well-preserved morphology described above but also in patches of highly degraded OM, as shown in the previous description of a breccia from these pegmatites (Franz et al., 2017). This OM is not only highly oxygenated (with up to 40 at. % O) but is also enriched in F ( $\leq 1.7$  at. %), Zr ( $\leq 7$  at. %), Sc ( $\leq 0.8$  at. %), Y ( $\leq 2.7$  at. %), and rare earth elements (sum  $\leq 0.35$  at. %) that were most probably derived from the pegmatitic environment.

What is striking in all observations is the close connection between kerite and fluorite, which was also described by Zhmur (2003). The whole occurrence in the granitic pegmatites with a large amount of topaz in the chambers (Lyckberg et al., 2019, report that a single pegmatite, no. 464, had produced 6 t of topaz in mining) points to a high concentration of F in the late-magmatic to hydrothermal fluids. In addition, we observed F-rich muscovite during the formation of the breccia (Franz et al., 2017), and this also points to the importance of F activity. This fluid likely carried a high amount of silica as  $\text{SiF}_4$  (plus other components, such as Al, alkalis, Ca, Mg, and Fe).

For the fossilization process we assume that this fluid was able to react with kerite at a depth of 1–2  $\mu\text{m}$  (Figs. 7–10). Gorlenko et al. (2000) and Zhmur (2003) described the outer part of the filaments as a former sheath of the microorganisms. We interpret this rim area as a former thin coating of biofilm that was probably very sensitive in an early stage of Si–Al infiltration, with Ca infiltration slightly deeper into kerite. The small mineralized structures on the surface of fil-

aments (Fig. 3c) resemble what Gorlenko et al. (2000) interpreted as membrane leaflets.

### 3.2 Environment of fossilization

The geological situation for the fossilization is summarized in Fig. 15. We assume that fossilization must have occurred during a hydrothermal event within a fluid that carried enough Si, Al, F, and Ca to react with the kerite degradation products in nano-environments. The Korosten pluton intruded into continental crust, and the geological situation indicates a long-living plutonic–volcanic activity (Shumlyanskyy et al., 2021), likely with near-surface geyser systems. The crystallization of the pegmatites and formation of the chambers occurred at a depth of 2 to 2.5 km (Lukashev, 1976; Kalyuzhnyi et al., 1971; Voznyak et al., 2012). The miarolitic cavities of the granite, possibly with periodical influx of hydrothermal waters, provided the space for a deep continental biosphere, consisting probably of anaerobic, thermophilic, and acidophilic microbial species. Methanogenic microbes (indicated by C and N stable isotopes; Franz et al., 2017) might have been an important part of such a cryptic endolithic micro-ecosystem in a continental, terrestrial environment.

The flaky kerite, also visible as thin films in cross section, point to the participation of biofilms in this ecosystem which might have developed as soon as the temperatures in the miarolitic chambers were sufficiently low for organisms to live in this environment. The essential components for the organisms – C, N, S, P – or the microorganisms themselves were transported with meteoric water from the surface to the chambers. Alternatively, the components for the organisms might have been transported from the metamorphic country rocks of the Korosten pluton into the chambers via hydrothermal convection cells (e.g., Bobos and Williams, 2017, who described  $\text{NH}_4$  transport for tobelite formation in a sedimentary basin).

Some of the miarolitic cavities collapsed and produced a breccia, which also contains degraded OM and black opal with inclusion of carbohydrates (Franz et al., 2017). Chambers which did not collapse must have been sealed. They contained a large amount of gas under high pressure, and the sealing preserved the gas from escape. Lyckberg et al. (2019) reported that old log books of the mining activities in Volyn describe an event in 1955, when at a depth of 600 m drilling penetrated a gas-filled cavity, and as a consequence the entire drill steel shot out of the hole and toppled the drill tower. It took more than 30 min before the highly pressurized gas slowed down. That a large amount of gas must have been produced during decay of the OM is also indicated by the fluid–solid equilibria between  $\text{NH}_4^+$  and  $\text{K}^+$ , responsible for the buddingtonite formation. It is known from experimental data that for the transformation of K-feldspar into buddingtonite,  $X_{\text{NH}_4}$  in the fluid must be very high (Pöter et al., 2004).

Laser-ablation dating with the  $^{39}\text{Ar}/^{40}\text{Ar}$  method of the muscovite from the breccia yielded an age of  $1491 \pm 9$  Ma, interpreted as the age of the hydrothermal breccia formation (Franz et al., 2022). Analyses of buddingtonite yielded an age range from  $383 \pm 12$  Ma to  $563 \pm 14$  Ma, and the oldest age of 563 Ma is interpreted as a minimum age because of probable Ar loss of the very fine-grained buddingtonite crystals. This minimum age is in the same range as the results of our attempt to date the fossils directly with Pb–Pb dating (Fig. 14). The maximum age is given by the intrusion age of the pegmatites,  $1760 \pm 3$  Ma (Fig. 1; Shumlyanskyy et al., 2021). The intrusion depth of 2 to 2.5 km might have been the depth for the microbial community, but there is a significant time lag between pegmatite formation (1.76 Ga) and the formation of the breccia (ca. 1.49 Ga) during which exhumation could have occurred.

Silicification of microbial organisms is typical for geyser systems, as shown by many recent analogues, e.g., for Yellowstone, USA (Cady and Farmer, 1996), Waitapu, New Zealand (Handley et al., 2008), and others (see references in Alleon et al., 2016). Consequently, a number of experimental studies on silicification of microorganisms including the processes of silica polymerization and precipitation in the presence of microorganisms were undertaken, starting with the earliest work by Oehler (1976). Experimental silicification of archaea (Orange et al., 2009) has shown that the outer surface layer of these organisms is the site for incipient silicification, and the ubiquity of biofilms on surfaces in hot springs (e.g., Cady and Farmer, 1996; Handley et al., 2008; Kremer et al., 2012) and other environments (Bortnikov et al., 2012) indicates the potential presence of biofilms also in the Precambrian at the subvolcanic geyser system in the Korosten pluton. Extracellular polymeric substances play an important role in silicification and fossilization as shown by many authors (see references above and therein), and fossilization of biofilms occurs very rapidly (Rozanov, 2003). After silicification of extracellular polymeric substances, clay minerals developed on the surface of the fossils from Volyn. This phenomenon was also observed in experimental studies (Urrutia and Beveridge, 1994) and in natural environments (Kremer et al., 2012; Bortnikov et al., 2012).

The formation of the 1–2  $\mu\text{m}$  thick layer of Si–Al infiltration and development of encrustations of Al silicates was essential for the excellent preservation of the morphology of the microfossils. The fossilization of organisms without skeletal parts requires special conditions which prevent autolysis. In fossilization experiments of crustacean eggs with phosphoric acid, Hippler et al. (2012) pointed out that rapid heating before treatment with phosphoric acid was essential for perfect preservation of the morphology of OM. This treatment denaturalized the proteins of the crustacean eggs, creating a stable template for mineralization which occurred rapidly within 1 to 2 weeks. We suspect a similar process for the silicification process at the Volyn locality. Anoxic conditions in the deep biosphere prevented early autolysis

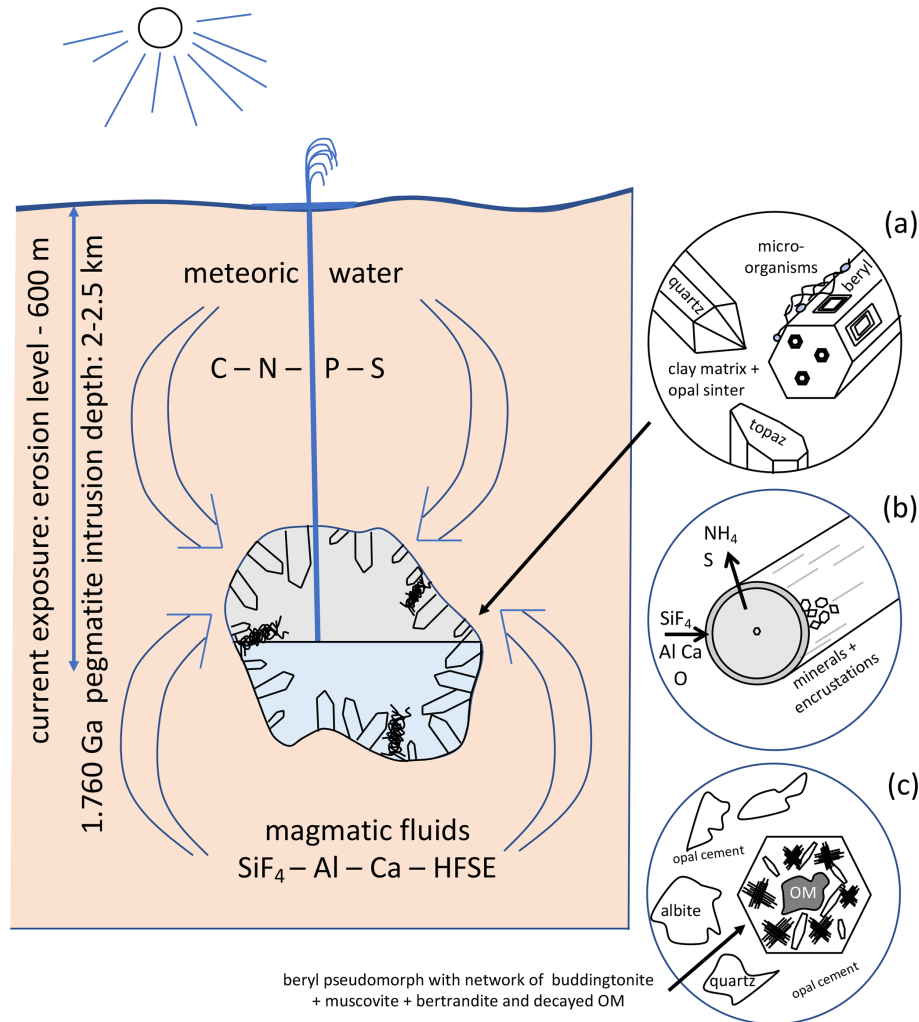


**Figure 15.** Schematic illustration of the geological environment of pegmatites of the Korosten pluton, Ukraine, with meter-sized miarolitic chambers and a near-surface geyser system. The chambers provided the space for an endolithic micro-ecosystem, which consists (a) of organisms with three morphologically different types (filamentous, flaky, and rare spherical), attached to the pegmatitic minerals, also in etch pits of beryl. (b) Fossilization occurs due to influx of hydrothermal fluids carrying SiF<sub>4</sub>, Al, Ca, and high-field-strength elements (HFSEs) and starts with a micrometer-thin layer of Al–Si enrichment, which develops into clay minerals, feldspar, and finally into encrustations. (c) Strongly degraded OM is found also in breccias, formed during collapse of some chambers, providing NH<sub>4</sub> for the formation of buddingtonite, together with muscovite and bertrandite, in pseudomorphs after beryl.

of the organisms, and then shock heating might have occurred due to influx of hot hydrothermal waters into the miarolitic caves, carrying SiF<sub>4</sub>, together with Al, Ca, and other elements, producing rapid infiltration of Si, Al, and Ca into the outer surface layer of the organisms, including precipitation of opal (Fig. 4f). The early envelope of silicification minimizes the molecular degradation of the fossils, as also shown experimentally by Alleon et al. (2016). Further heating (without deformation) after formation of the Si–Al-enriched outer rim enhanced the decay but did not destroy the morphology. Kremer et al. (2012) pointed out that the morphology of calcified cyanobacteria was destroyed, whereas silicification, when rapid, helps to preserve their morpholog-

ical details (e.g., Bartley, 1996; Manning-Berg et al., 2019, and references therein). That fossilization of bacterial organisms is a rapid process has also been postulated by Rozanov (2003). Raff et al. (2008) demonstrated experimentally that under anoxic conditions (preventing autolysis) rapid formation of bacterially induced biofilms on the surface of organisms provided the site for early mineralization with Ca minerals. These biofilm bacteria induce a catalyzing process for rapid fine-grained mineralization, which was also postulated by Briggs (2003). Extracellular polymeric substances are known to provoke diagenetic mineralization, possibly as the result of liberation of adsorbed cations during degradation (Arp et al., 1999; Dupraz and Visscher, 2005; Altermann

et al., 2006). Notably, most of the cases described in the literature and quoted above deal with marine environments, whereas the case reported here deals with a Precambrian continental, subsurface environment. Only in the continental environment are fluids rich in F present; in the oceanic environment granites are much less abundant than mafic rocks, and they commonly lack F-enriched pegmatites.

The extracellular biosilicification capability of bacteria and archaea in geothermal environments with transformation of soluble  $\text{Si}(\text{OH})_4$  into nanoscale  $\text{SiO}_2$  precipitates on the surface has recently been emphasized by Ikeda (2021). Bacteria, such as *Thermus thermophilus* (Iwai et al., 2010), can form siliceous deposits from supersaturated solutions in biofilms on the outer surface layer of the cell envelope.

Zhmur (2003), based on the data by Gorlenko et al. (2000) and by comparison with other occurrences in igneous rocks and in recent geyser environments, proposed a hydrothermal origin of cyanobacteria and microbial bio-mats in geyser ponds for the Volyn occurrence. The fossilization occurred in situ in zones of silica precipitation, forming sealed cup-like structures. The floating cyanobacterial mat was buried in the self-sealed biogenic-geyser structure that was formed at the hydrothermal discharge site, and the collapse of these structures produced the breccia observed at the Volyn deposit. This model implies that the fossils were transported downward with the geyser water to the chambers because photosynthesizing cyanobacteria must have lived at the surface. This is not consistent with our observations, which show that the filaments, together with irregular and spherical kerite, grew onto and into the etch pits of beryl (Fig. 3a). If transport had occurred, this would have probably destroyed the delicate filaments, producing a mat-like OM, such as that described by Zhmur (2003).

#### 4 Concluding remarks

The pegmatitic Volyn kerite occurrence is probably one of the localities world-wide with the best-preserved Precambrian microfossils. Common occurrences of (Precambrian) fossils are in sedimentary rocks, especially in chert, but there is growing evidence of OM in the pore space of igneous rocks (Ivarsson et al., 2020). Several factors have contributed to the micro-taphonomical process to preserve the Volyn fossils as part of an endolithic micro-ecosystem. First, the chambers in the pegmatites provided an exceptionally large “pore” space. Secondly, water was present in such an environment, necessary for life, although this space was not necessarily completely water-filled but was possibly a cavity with temporary changes in the water level. Transport of Si was likely enhanced by F, present in this pegmatitic, granitic environment. OM would have decayed, when O was available, hence silicification of the outer parts of the kerite fossils implies rapid reaction with Si and shielding for access of O. This environment in the deep biosphere was similar to geyser systems,

which are known to be sites of preferred microbial growth. The microorganisms contribute to the microstructural development of geysers by providing a favored substrate for opaline silica precipitation, and encrustation and degradation of microorganisms are the dominant modes of fossilization at the high temperature end of the geyser system (Cady and Farmer, 1996).

There is growing awareness of the importance of life in the deep igneous biosphere especially in the record of early life, the most important reservoir of biomass in the Precambrian (Ivarsson et al., 2020). The presence of F-rich hydrothermal waters in the late stage of granitic, subvolcanic plutons might be a common scenario for preservation of microorganisms, without the later influence of deformation and metamorphism, such as in chert, where most of the studies of Precambrian fossils have been undertaken. Granitic rocks might be sites for the very early diagenetic emplacement of silica, leading to 3D preservation of non-biomineralizing fossils, the “Bitter Springs-type preservation” (Butterfield, 2003). The search for indications of early life, and its evolution during the Precambrian, has concentrated mainly on submarine hydrothermal vents (e.g., Dodd et al., 2017), but it should be extended also to terrestrial environments.

*Data availability.* All data are in the paper or in the Supplement.

*Supplement.* The supplement related to this article is available online at: <https://doi.org/10.5194/bg-19-1795-2022-supplement>.

*Author contributions.* GF developed the concept and did the writing, PL, VC, and VK did the sampling and reviewing of the manuscript, H-MS provided the data for reflected light microscopy and reviewed the manuscript, NM provided data for open-system pyrolysis, RW provided data for TEM, JG did all isotope investigations for radiometric dating, and UG was responsible for SEM and JN for EMPA.

*Competing interests.* The contact author has declared that neither they nor their co-authors have any competing interests.

*Disclaimer.* Publisher’s note: Copernicus Publications remains neutral with regard to jurisdictional claims in published maps and institutional affiliations.

*Acknowledgements.* We thank Anja Schreiber for preparation of FIB foils and Dorothee Hippler for comments on an earlier version, two anonymous reviewers for their careful and helpful reviews, and Tina Treude for editorial handling.

*Financial support.* This research has been supported by the Technische Universität Berlin (Akademisches Auslandsamt grant).

This open-access publication was funded by Technische Universität Berlin.

*Review statement.* This paper was edited by Tina Treude and reviewed by two anonymous referees.

## References

- Alleon, J., Bernard, S., Le Guillou, C., Daval, D., Skouri-Panet, F., Pont, S., Delbes, L., and Robert, F.: Early entombment within silica minimizes the molecular degradation of microorganisms during advanced diagenesis, *Chem. Geol.*, 437, 98–108, 2016.
- Altermann, W., Kazmierczak, J., Oren, A., and Wright, D. T.: Cyanobacterial calcification and its rock-building potential during 3.5 billion years of Earth history, *Geobiology*, 4, 147–166, 2006.
- Arp, G., Reimer, A., and Reitner, J.: Calcification in cyanobacterial biofilms of alkaline salt lakes, *Eur. J. Phycol.*, 34, 393–403, 1999.
- Bartley, J. K.: Actualistic taphonomy of cyanobacteria: implications for the Precambrian fossil record, *Palaios*, 571–586, 1996.
- Burnham, A. K. and Sweeney, J. J.: A chemical kinetic model of vitrinite maturation and reflectance, *Geochim. Cosmochim. Ac.*, 53, 2649–2657, 1989.
- Butterfield, N. J.: Exceptional fossil preservation and the Cambrian explosion, *Integr. Comp. Biol.*, 43, 166–177, 2003.
- Bobos, I. and Williams, L. B.: Boron, lithium and nitrogen isotope geochemistry of  $\text{NH}_4$ -illite clays in the fossil hydrothermal system of Harghita Băi, East Carpathians, Romania, *Chem. Geol.*, 473, 22–39, 2017.
- Bortnikov, N. S., Novikov, V. M., Soboleva, S. V., Savko, A. D., Boeva, N. M., Zhegallo, E. A., and Bushueva, E. B.: The role of organic matter in the formation of fireproof clay of the Latnenskoe Deposit, *Dokl. Earth Sci.*, 444, 634–639, 2012.
- Briggs, D. E. G.: The role of decay and mineralization in the preservation of soft-bodied fossils, *Annu. Rev. Earth Pl. Sc.*, 31, 275–301, 2003.
- Cady, S. L. and Farmer, J. D.: Fossilization processes in siliceous thermal springs: trends in preservation along thermal gradients, *Evolution of hydrothermal ecosystems on Earth and Mars?*, Chichester (Ciba Foundation Symposium 202), Wiley, 150–173, 1996.
- Dodd, M. S., Papineau, D., Grenne, T., Slack, J. F., Rittner, M., Pirajno, F., O'Neill, J., and Little, C. T.: Evidence for early life in Earth's oldest hydrothermal vent precipitates, *Nature*, 543, 60–64, 2017.
- Dormans, H. N. M., Huntgens F. J., and van Krevelen D. W.: Chemical structure and properties of coal: 20. Composition of the individual macerals, *Fuel*, 36, 321–339, 1957.
- Dupraz, C. and Visscher, P. T.: Microbial lithification in marine stromatolites and hypersaline mats, *Trends Microbiol.*, 13, 429–438, 2005.
- England, W. and Mackenzie, A.: Some aspects of the organic geochemistry of petroleum fluids, *Geol. Rundsch.*, 78, 291–303, 1989.
- Franz, G., Khomenko, V., Vishnyevskyy, A., Wirth, R., Struck, U., Nissen, J., Gernert, U., and Rocholl, A.: Biologically mediated crystallization of buddingtonite in the Paleoproterozoic: Organic-igneous interactions from the Volyn pegmatite, Ukraine, *Am. Mineral.*, 10, 2119–2135, 2017.
- Franz, G., Sudo, M., and Khomenko, V.:  $^{40}\text{Ar}/^{39}\text{Ar}$  dating of a hydrothermal pegmatitic buddingtonite-muscovite assemblage from Volyn, Ukraine, *Eur. J. Mineral.*, 34, 7–21, 2022.
- Ginzburg, A. I., Bulgakov, V. S., Vasilishin, I. S., Luk'yanova, V. T., Solntseva, L. S., Urmenova, A. M., and Uspenskaya, V. A.: Kerite from pegmatites of Volyn, *Dokl. Akad. Nauk SSSR+*, 292, 188–191, 1987 (in Russian).
- Gorlenko, V. M., Zhmur, S. I., Duda, V. I., Osipov, G. A., Suzina, N. E., and Dmitriev, V. V.: Fine structure of fossilized bacteria in Volyn kerite, *Origin of Life and Evolution of the Biosphere*, 30, 567–577, 2000.
- Handley, K. M., Turner, S. J., Campbell, K. A., and Mountain, B. W.: Silicifying biofilm exopolymers on a hot-spring microstromatolite: templating nanometer-thick laminae, *Astrobiology*, 8, 747–770, 2008.
- Hippler, D., Hu, N., Steiner, M., Scholtz, G., and Franz, G.: Experimental mineralization of crustacean eggs: new implications for the fossilization of Precambrian–Cambrian embryos, *Biogeosciences*, 9, 1765–1775, <https://doi.org/10.5194/bg-9-1765-2012>, 2012.
- Horsfield, B.: Practical criteria for classifying kerogens: Some observations from pyrolysis-gas chromatography, *Geochim. Cosmochim. Ac.*, 53, 891–901, 1989.
- Ikeda, T.: Bacterial biosilicification: a new insight into the global silicon cycle, *Biosci. Biotech. Bioch.*, 85, 1324–1331, 2021.
- Ivanovich, P. V. and Alekseevich, D. S.: Mineralogy of the Volynian chamber pegmatites, *Mineral. Almanac*, 12, EKOST Association, Moscow, ISBN 5-9900395-42-1, 128 pp., 2007.
- Ivarsson, M., Drake, H., Neubeck, A., Sallstedt, T., Bengtson, S., Roberts, N. M. W., and Rasmussen, B.: The fossil record of igneous rocks, *Earth-Sci. Rev.*, 210, <https://doi.org/10.1016/j.earscirev.2020.103342>, 2020.
- Iwai, S., Doi, K., Fujino, Y., Nakazono, T., Fukuda, K., Motomura, Y., and Ogata, S.: Silica deposition and phenotypic changes to *Thermus thermophilus* cultivated in the presence of supersaturated silica, *ISME J.*, 4, 809–816, 2010.
- Kalyuzhnyi V. A., Voznyak, D. K., and Gigashvili, G. M.: Mineral-forming fluids and mineral paragenesis of chamber pegmatites of Ukraine, *Naukova Dumka, Kyiv*, 216 pp., 1971 (in Ukrainian).
- Kremer, B., Kazmierczak, J., Lukomska-Kowalczyk, M., and Kempe, S.: Calcification and silicification: fossilization potential of cyanobacteria from stromatolites of Niuafu'ou's Caldera Lakes (Tonga) and implications for the early fossil record, *Astrobiology*, 12, 535–548, 2012.
- Larter, S. R.: Application of analytical pyrolysis techniques to kerogen characterisation and fossil fuel exploration/exploitation, in: *Analytical pyrolysis, methods and applications*, edited by: Voorhees, K., Butterworth, London, 212–275, 1984.
- Lukashev, A. N.: Depth of pegmatite formation, *Nedra, Moscow*, 152 pp., 1976 (in Russian).
- Lu'kyanova, V. T., Lobzova, R. V., and Popov, V. T.: Filaceous kerite in pegmatites of Volyn, *Izv. Ross. Akad. Nauk Ser. Geologicheskaya*, 5, 102–118, 1992 (in Russian).

- Lyckberg, P., Chernousenko, V., and Wilson, W. E.: Famous mineral localities: Volodarsk-Volynski, Zhitomir Oblast, Ukraine, *Mineral. Rec.*, 40, 473–506, 2009.
- Lyckberg, P., Chournousenko, V., and Chournousenko, O.: Giant heliodor and topaz pockets of the Volodarsk chamber pegmatites, Korosten pluton, Ukraine, 36th Intern. Gemm. Conf., 27–31 August 2019, Nantes, France, 78–83, 2019.
- Mahlstedt, N., di Primio, R., and Horsfield, B.: On the shale gas potential of the Georgina Basin, Record 2014 Geoscience Australia, Canberra, <http://pid.geoscience.gov.au/dataset/ga/146378>, 2014.
- Mahlstedt, N., di Primio, R., Horsfield, B., and Boreham, C. J.: Multi-component kinetics and late gas potential of selected Cooper Basin source rocks, Record 2015/19 Geosci. Australia, Canberra, 199 pp., <https://doi.org/10.11636/Record.2015.019>, 2015.
- Manning-Berg, A. R., Wood, R. S., Williford, K. H., Czaja, A. D., and Kah, L. C.: The taphonomy of proterozoic microbial mats and implications for early diagenetic silicification, *Geosci.*, 9, 40, 2019.
- Oberlin, A., Boulmier J. L., and Durand B.: Electron microscope investigation of the structure of naturally and artificially metamorphosed kerogen, *Geochim. Cosmochim. Ac.*, 38, 647–650, 1974.
- Oehler, J. H.: Experimental studies in Precambrian paleontology: structural and chemical changes in blue-green algae during simulated fossilization in synthetic chert, *Geol. Soc. Am. Bull.*, 87, 117–129, 1976.
- Orange, F., Westall, F., Disnar, J. R., Prieur, D., Bienvenu, N., Le Romancer, M., and Défarge, C.: Experimental silicification of the extremophilic Archaea *Pyrococcus abyssi* and *Methanocaldococcus jannaschii*: applications in the search for evidence of life in early Earth and extraterrestrial rocks, *Geobiology*, 7, 403–418, 2009.
- Poetz, S., Horsfield, B., and Wilkes, H.: Maturity-driven generation and transformation of acidic compounds in the organic-rich Posidonia Shale as revealed by electrospray ionization Fourier transform ion cyclotron resonance mass spectrometry, *Energy Fuels*, 28, 4877–4888, 2014.
- Pöter, B., Gottschalk, M., and Heinrich, W.: Experimental determination of ammonium partitioning among muscovite, K-feldspar, and aqueous chloride solutions, *Lithos*, 74, 67–90, 2004.
- Quigley, T. M. and Mackenzie, A. S.: The temperatures of oil and gas formation in the sub-surface, *Nature*, 333, 549–552, 1988.
- Radke, M., Horsfield, B., Littke, R., and Rullkötter, J.: Maturation and petroleum generation, in: *Petroleum and Basin Evolution: Insights from Petroleum Geochemistry, Geology and Basin Modeling*, edited by: Welte, D. H., Horsfield, B., and Baker, D. R., Springer Verlag, Berlin, Heidelberg, 169–229, 1997.
- Raff, E. C., Schollaert, K. L., Nelson, D. E., Donoghue, P. C., Thomas, C. W., Turner, F. R., and Raff, R. A.: Embryo fossilization is a biological process mediated by microbial biofilms, *P. Natl. Acad. Sci. USA*, 105, 19360–19365, 2008.
- Rožanov, A. Yu.: Fossil bacteria, sedimentogenesis, and the early biospheric evolution, *Paleontol. Zh.*, 6, 41–49, 2003 [*Paleontol. J.*, 37, 600–608 (2003)].
- Shumlyanskyy, L., Belousoca, E., and Petrenko, O.: Geochemistry of zircons from basic rocks of the Korosten anorthosite-mangerite-charnockite-granite complex, northwestern region of the Ukrainian Shield, *Miner. Petrol.*, 111, 459–466, 2017.
- Shumlyanskyy, L., Franz, G., Glynn, S., Mytrokhyn, O., Voznyak, D., and Bilan O.: Geochronology of granites of the western part of the Korosten AMCG complex (Ukrainian Shield): implications for the emplacement history and origin of miarolitic pegmatites, *Eur. J. Mineral.*, 33, 703–716, 2021.
- Sinninghe Damsté, J. S., Eglinton, T. I., De Leeuw, J. W., and Schenck, P. A.: Organic sulphur in macromolecular sedimentary organic matter: I. Structure and origin of sulphur-containing moieties in kerogen, asphaltene and coal as revealed by flash pyrolysis, *Geochim. Cosmochim. Ac.*, 53, 873–889, 1989.
- Tahán, J. E., Granadillo, V. A., Sánchez, J. M., Cubillán, H. S., and Romero, R. A.: Mineralization of biological materials prior to determination of total mercury by cold vapour atomic absorption spectrometry, *J. Anal. Atom. Spectrom.*, 8, 1005–1010, 1993.
- Tissot, B. P. and Welte, D. H.: *Petroleum formation and occurrence*, 2nd edn., Springer-Verlag, Berlin, [https://doi.org/10.1007/978-3-642-87813-8\\_1](https://doi.org/10.1007/978-3-642-87813-8_1), 1984.
- Urrutia, M. M. and Beveridge, T. J.: Formation of fine-grained metal and silicate precipitates on a bacterial surface (*Bacillus subtilis*), *Chem. Geol.*, 116, 261–280, 1994.
- Vermesch, P.: IsoplotR: a free and open toolbox for geochronology, *Geosci. Front.*, 9, 1479–1493, <https://doi.org/10.1016/j.gsf.2018.04.001>, 2018.
- Voznyak, D. K., Khomenko, V. M., Franz, G., and Wiedenbeck, M.: Physico-chemical conditions of the late stage of Volyn pegmatite evolution: Fluid inclusions in beryl studied by thermobarometry and IR-spectroscopy methods, *Mineral. J. (Ukraine)*, 34, 26–38, 2012 (in Ukrainian).
- Wirth, R.: Focused Ion Beam (FIB): a novel technology for advanced application of micro- and nanoanalysis in geosciences and applied mineralogy, *Eur. J. Mineral.*, 16, 863–876, 2004.
- Wirth, R.: Focused ion beam (FIB) combined with SEM and TEM: Advanced analytical tools for studies of chemical composition, microstructure and crystal structure in geomaterials on a nanometre scale, *Chem. Geol.*, 261, 217–229, 2009.
- Zhmur, S. I.: Origin of Cambrian fibrous kerites of the Volyn region, *Lithol. Miner. Resour.*, 38, 55–73, 2003.